

RESEARCH ARTICLE

Analysis of the transitional flow field over a fixed hummingbird wing

Yossef Elimelech* and Charles P. Ellington

University of Cambridge, Department of Zoology, Downing Street, Cambridge CB2 3EJ, UK

*Author for correspondence at present address: Technion – Israel Institute of Technology, Faculty of Aerospace Engineering, Haifa 32000, Israel (yosie@aerodyne.technion.ac.il)

SUMMARY

We analyzed the flow fields characterized by chord-based Reynolds numbers of 5000 to 15,000 over a stationary model of a hummingbird (*Calypte anna*) wing. Utilizing two experimental techniques, constant-temperature anemometry and stereo particle image velocimetry, the high-fidelity results depict a laminar-to-turbulent transition process that develops over the wing. At both zero and non-zero angles of attack the spectrum of the velocity signals is wide. At non-zero angles of attack the flow separates from the wing surface and a shear layer forms. As a result, unsteady flow disturbances amplify at a chord-based Reynolds numbers as low as 5000. Nevertheless, only at a Reynolds number of 15,000 is the flow disturbance growth rate sufficient to bring enough momentum from the outer region of the boundary layer to reattach the flow to the wing surface. For a Reynolds number of 5000, a comparison between the observed growth rates and a theoretical approximation concludes that flow disturbances of a Strouhal number of unity (and above) are no longer two-dimensional. In view of these conclusions, this study could serve as the first step towards a better understanding of the flow mechanisms over steady revolving and periodically flapping wings at this Reynolds number regime.

Key words: laminar-to-turbulent transition, separation-induced transition, low Reynolds number flow, aerodynamics, hummingbird flight.

Received 24 May 2012; Accepted 5 September 2012

INTRODUCTION

Since Weis-Fogh's (Weis-Fogh, 1973) pioneering analysis of hovering animal flight, it has generally been assumed that the flow mechanisms that govern hummingbirds' aerodynamics are the same as those of insects. Our understanding of insect flight mechanisms has advanced greatly during the last two decades; many efforts have focused on obtaining the flow field over periodically flapping and steady rotating wings since the quasi-state assumption (at the appropriate Reynolds numbers) failed to produce enough aerodynamic force to support the maneuvering capabilities of insects (Ellington, 1984).

These efforts yielded identification of several high-lift flow mechanisms; over insect wings, most of the lift is associated with a large, stable leading-edge vortex that separates from the sharp leading edge of the wing (Ellington et al., 1996; Van den Berg and Ellington, 1997). Other aspects of this leading-edge vortex, such as its spanwise distribution (Bomphrey et al., 2005) and its stability (Lentink and Dickinson, 2009; Maxworthy, 2007), are more controversial. Usherwood and Ellington (Usherwood and Ellington, 2002) showed that the leading-edge vortex is stable on wings steadily rotating like a propeller. The resultant aerodynamic force is normal to the wing surface, reflecting the fact that the leading-edge vortex essentially eliminates the leading-edge suction. The practical meaning of this result is that the low lift-to-drag ratio can be approximated as $L/D \sim \cot(\alpha')$ where L and D are the aerodynamic lift and drag, respectively, and α' is the wing's geometric angle of attack. Therefore, high vertical force coefficients, measured in propeller tests for various aspect ratios and Reynolds numbers, were inevitably associated with high aerodynamic drag.

Other flow mechanisms were proposed by Weis-Fogh (Weis-Fogh, 1973) for wing rotation at each end of the half-stroke. Weis-Fogh distinguished between the clap and the fling; the former relates to the two wings coming together, with the first contact made at the leading edges. Maxworthy (Maxworthy, 1981) showed that such a contact process produces a downward jet so that in reaction, the wings experience an upward force. The fling occurs when the wings separate from one another at the beginning of the down-stroke; the leading edges separate first, leaving the trailing edges still in contact. Weis-Fogh hypothesized that during the fling, air flows into the expanding gap between the wings to create circulation about each wing, thus increasing the force it generates. This hypothesis was tested and verified by several authors (Bennett, 1966; Maxworthy, 1979; Maxworthy, 1981; Spedding and Maxworthy, 1986).

Many experimental and numerical studies on insect flight mechanisms were carried out at Reynolds numbers of laminar flow and it is tempting to apply the leading-edge vortex mechanism indiscriminately to hummingbirds. Most insects hover at a mean chord-based Reynolds number less than 5000; the largest insects approach 10^4 (Ellington, 2006). Ellington and Usherwood (Ellington and Usherwood, 2001) extended the experimental methods to Reynolds numbers between 10,000 and 50,000. They concluded that the lift enhancement from a large leading-edge vortex is destroyed by transition to turbulent flow at Reynolds numbers as low as 10,000. However, other studies have reported a vorticity concentration over a model of swift wings (Videler et al., 2004) and over bats (Edmonds, 2005; Muijres et al., 2008), which indicates a leading-edge vortex lift enhancement mechanism beyond the low Reynolds number regime that characterizes insects. These contradicting observations make hummingbirds especially interesting because

their characteristic chord-based Reynolds number during hovering ranges from 5000 to 20,000 (Altshuler et al., 2004). It is not known whether they operate at both laminar and turbulent flow regimes. There are no apparent structural features on hummingbird wings that distinguish one Reynolds number regime from the other. Several morphological aspects such as wing camber, thickness and a non-zero leading-edge radius suggest that they do not operate in the laminar flow regime. Nevertheless, we are not confident whether the integral aerodynamic characteristics of such wings reflect an attached turbulent flow. At Reynolds numbers in the range of 5000 to 20,000, a stable leading-edge vortex may not exist or is considerably reduced in size and in effect due to turbulent mixing. Therefore, the state of the leading-edge vortex may serve as an indicator that can distinguish between a laminar and fully turbulent flow field. This collection of reasons led us to hypothesize that the flow mechanisms over hummingbird wings do not necessarily include a steady leading-edge vortex like the one that appears over insect wings in the laminar flow regime. As matter of fact, flow separation and disturbance growth are likely to occur in this transitional Reynolds number regime. In that case, the laminar separation bubble is probably unstable and incorporates vortex shedding, unsteady mixing and, in some cases, turbulent reattachment. A detailed and critical inspection of the flow is essential, because even an unsteady flow field (i.e. no stable leading-edge vortex) may show a time-averaged flow over a three-dimensional separation bubble that results in aerodynamic characteristics that are analogous to those of a stable leading-edge vortex.

This study is the first direct examination of the flow field over hummingbird wings. We utilized a simplistic approach that analyzes the flow over a hummingbird wing in steady rectilinear flow at a few Reynolds numbers of biological relevance. Because hummingbirds produce higher lift during the down-stroke (Warrick et al., 2005; Warrick et al., 2009), this study focuses on this phase of the flapping wing cycle. Such a naive approach may serve as a first step towards a flow analysis over rotating and flapping wings in this Reynolds number regime.

We hope to gain insight about the main flow mechanisms involved and how these relate to the wing morphology. Because proper analysis of transitional flow mechanisms is still challenging for most, if not all, numerical methodologies, an experimental approach was adopted. Flow measurements were conducted over a

hummingbird wing model; high-resolution velocity profiles were obtained using constant-temperature anemometry (CTA). Complementary stereo particle image velocimetry (SPIV) measurements allowed a global understanding of the flow field and identification of flow structures. A similar in-depth analysis over a steady rotating or flapping wing is not yet practically feasible.

MATERIALS AND METHODS

Wing model

A dried wing of a male Anna's hummingbird [*Calypte anna* (Lesson 1829)] was placed in a custom-built laser scanner to obtain its three-dimensional profile (Ng, 2010). Within the large family of hummingbirds, this species is medium-sized; it has an average adult body length of ~100 mm, a wingspan ranging from 114 to 121 mm and an average mass of ~4.25 g. The wing morphology is shown in Fig. 1. The bone region extends from the wing root up to 40% of the wing length, and is characterized by highly cambered cross-sections (Fig. 1) and a large leading-edge radius. Coverts that cover the bone in this region create a rough texture in the leading-edge region, but this is likely to be an artifact of the dried skin. Along more distal locations, the cross-sections become flatter and an asymmetric feather (the primary 10th feather) constructs a sharp leading edge.

Using these morphological data, a 4:1 scaled wing model was designed (wing length of 200 mm). The wing was fabricated using stereo lithography (VeroBlack, Objet, Rehovot, Israel), yielding a rigid and non-porous wing model. Scanning electron microscopy (SEM) of the *C. anna* wing revealed that under no loading the feathers are not porous (Fig. 2); the gaps are so small compared with the boundary layer thickness that the wing is probably impermeable. Moreover, the SEM scans indicated a physical connection between adjacent barbs. Restricting the following analysis to the down-stroke (in which wing deformation is minimal) together with the results of the SEM scans justified the use of a non-porous wing model in the following analysis.

Test facility and flow conditions

The experiments were conducted in the low-speed wind tunnel located at the Faculty of Aerospace Engineering at the Technion (Israel Institute of Technology, Haifa, Israel). The tunnel operates in a closed loop and is driven by a vane-axial fan. The inlet has a contraction ratio of 5.76:1; the test section length is 1.35 m and the cross-section

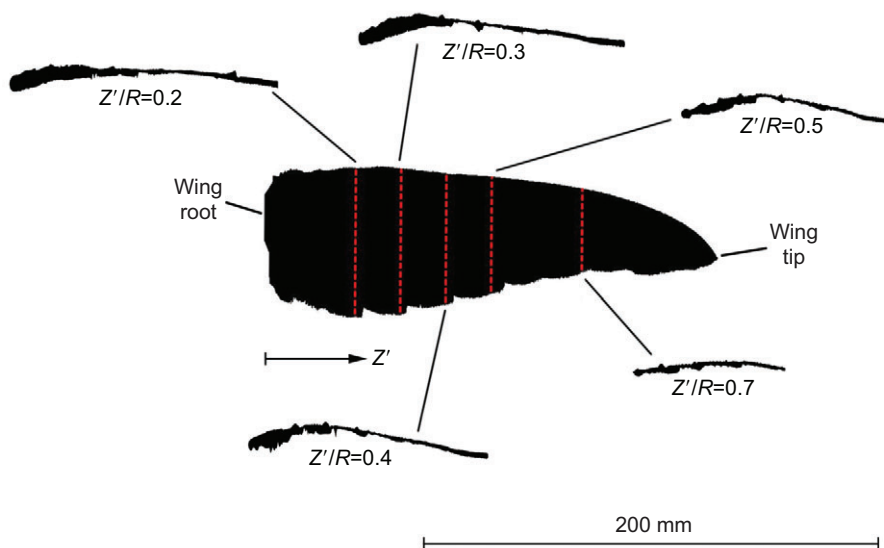


Fig. 1. Hummingbird wing model planform and representative cross-sections. The cross-sections are shown at an angle of attack of the wing of 0 deg.

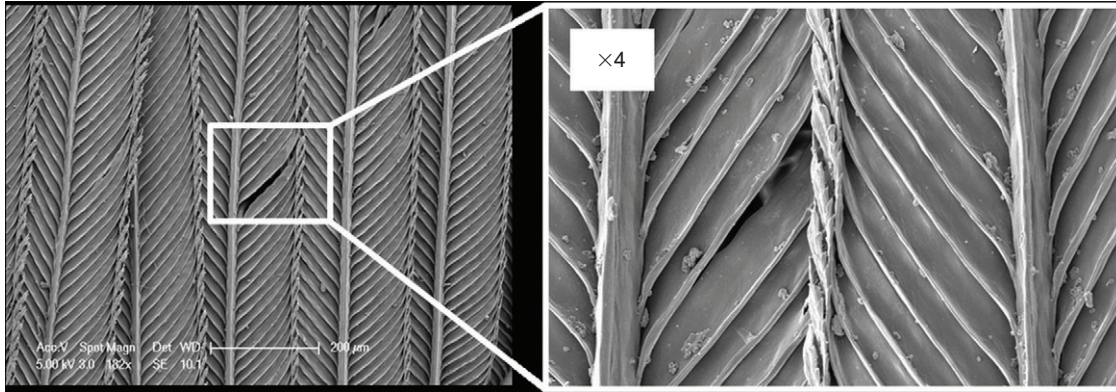


Fig. 2. Scanning electron microscope image of the *Calypte anna* wing. The right panel is a fourfold magnification of the white-bordered region that appears in the left panel.

dimensions are 0.5×0.5 m. The experiments were conducted at a free-stream velocity between 1.6 and 5 m s^{-1} . The low free-stream velocity, derived from the Reynolds numbers under investigation (given the wing's mean aerodynamic chord), yielded a low dynamic pressure, which did not allow us to measure the aerodynamic loads on the wing model. During tests, the free-stream velocity was kept within 1%, and the turbulence intensity (corresponding to 0.1 to 500 Hz frequency range) varied between 0.05 and 0.15% . Most of the energy of the free-stream velocity fluctuations is concentrated in the lower-frequency band of the spectrum, below $\sim 4 \text{ Hz}$.

The wind-tunnel model was of a single wing, mounted on an inner sidewall, or end-plate, which served as a reflecting boundary. This end-plate isolated the wing from the wind-tunnel walls, which are characterized by thick boundary layers and high turbulence intensities. The length of the single wing is $R=200 \text{ mm}$ and its characteristic length scale is the mean aerodynamic chord, $\bar{c}=45 \text{ mm}$.

Hummingbirds operate at Reynolds numbers between 5000 and $20,000$ (Tobalske et al., 2007; Warrick et al., 2009). Analysis of their three-dimensional flight kinematics (Tobalske et al., 2007) showed that the stroke amplitude, the wing geometric angle of attack and the body angle are functions of the center-of-mass velocity with respect to the surrounding air (i.e. flight velocity assuming no wind); it also quantified the wing geometric angle of attack, which varies during the flapping cycle. Tobalske and colleagues showed that during rectilinear motion (velocity of 12 m s^{-1} , in this particular example) the chord orientation is $\sim 17 \text{ deg}$ below the flight path. Taking into account the velocity of the flapping wing (at mid-span), the chord angle of attack is $\sim 9 \text{ deg}$ at mid-stroke. Moreover, the same study showed that during hovering flight the geometric angle of attack at the middle of the down-stroke is $\sim 25 \text{ deg}$. Based on the physical properties of the bird, such as mass, wing span and flapping frequency, we applied the actuation disk approximation (Pennycuik, 1975) in order to evaluate the aerodynamic angle of attack at mid-stroke, yielding values between 10 and 20 deg at mid-span.

In order to obtain results at flow conditions of biological relevance, data was acquired at free-stream velocities of 1.67 , 3.34 and 5 m s^{-1} , which correspond to Reynolds numbers of 5000 , $10,000$ and $15,000$, respectively. The model angle of attack varied from zero incidence up to 10 deg ; for brevity, results will be presented only at the two extremes, 0 and 10 deg . As detailed above, it is understood that these test conditions represent the realistic flow conditions at the middle of the down-stroke during forward flight.

The results for the smallest angle of attack served as a quantitative reference and were compared with the results of a previous study that focused on the flow mechanisms over classic wings at this

Reynolds number regime (Elimelech, 2010). To follow the evolution of the laminar-to-turbulent transition process, the angle of attack was gradually increased by discrete steps of 5 deg . As will be described below, the results show that the flow field was highly unsteady for an angle of attack as low as 10 deg . The fact that this angle is also the smallest angle of attack during hovering flight (at mid-stroke) allowed us to restrict our analysis to this angle because the separated flow region is expected to be larger and less stable at higher angles of attack.

Constant-temperature anemometry

Historically, the main experimental technique in turbulence research is CTA. It is a mature experimental technique and is well documented (e.g. Bruun, 1996). The main advantage of CTA is its wide bandwidth ($\sim 10 \text{ kHz}$ at flow velocities of a few meters per second), which makes it suitable for spectral analysis. The main drawback of CTA is its intrusiveness. To minimize the intrusive effects, the sensor was positioned in the flow using a forward-facing sting, 450 mm long and 4 mm in diameter (Fig. 3A). Using temperature-sensitive paint (Elimelech, 2010), it has been verified that this arrangement indeed has no effect on the flow over the wing. We used the Dantec Streamline system, the TSI 1155-18 probe support and the Dantec 55P11 and TSI-1260A-T1.5 CTA sensors (Dantec Dynamics, Skovlunde, Denmark). These are one-dimensional sensors and hence they only allow measurement of the total velocity magnitude, V , in the plane perpendicular to the sensor. At velocities of the order of 0.1 m s^{-1} , the convection currents created by the heated sensor affect the flow field and the measurement (Bruun, 1996). Thus, we deem 0.1 m s^{-1} as the lowest reliable velocity measured in our experiments.

During all tests, the free-stream velocity signal and the signal within the boundary layer were acquired simultaneously. Each CTA measurement was a time-accurate record of 2^{16} acquisition points, sampled at 10 kHz (during 6.5 s). To avoid aliasing, a low-pass analog filter with a cut-off frequency of 3 kHz was applied prior to the analog-to-digital conversion. Integral characteristics of the signals, i.e. their respective mean values and standard deviations, were used to show the main flow features in the volume under examination. Additional signal processing was implemented using standard MATLAB (The MathWorks, Natick, MA, USA) routines such as `pwelch` and `periodogram` to obtain auto spectral densities.

To facilitate comparison between different tests, the instantaneous velocity measured in the vicinity of the wing, V , as well as that measured in the free stream, U , will be universally referenced to the time-averaged (over the measurement interval) value of the latter, \bar{U} .

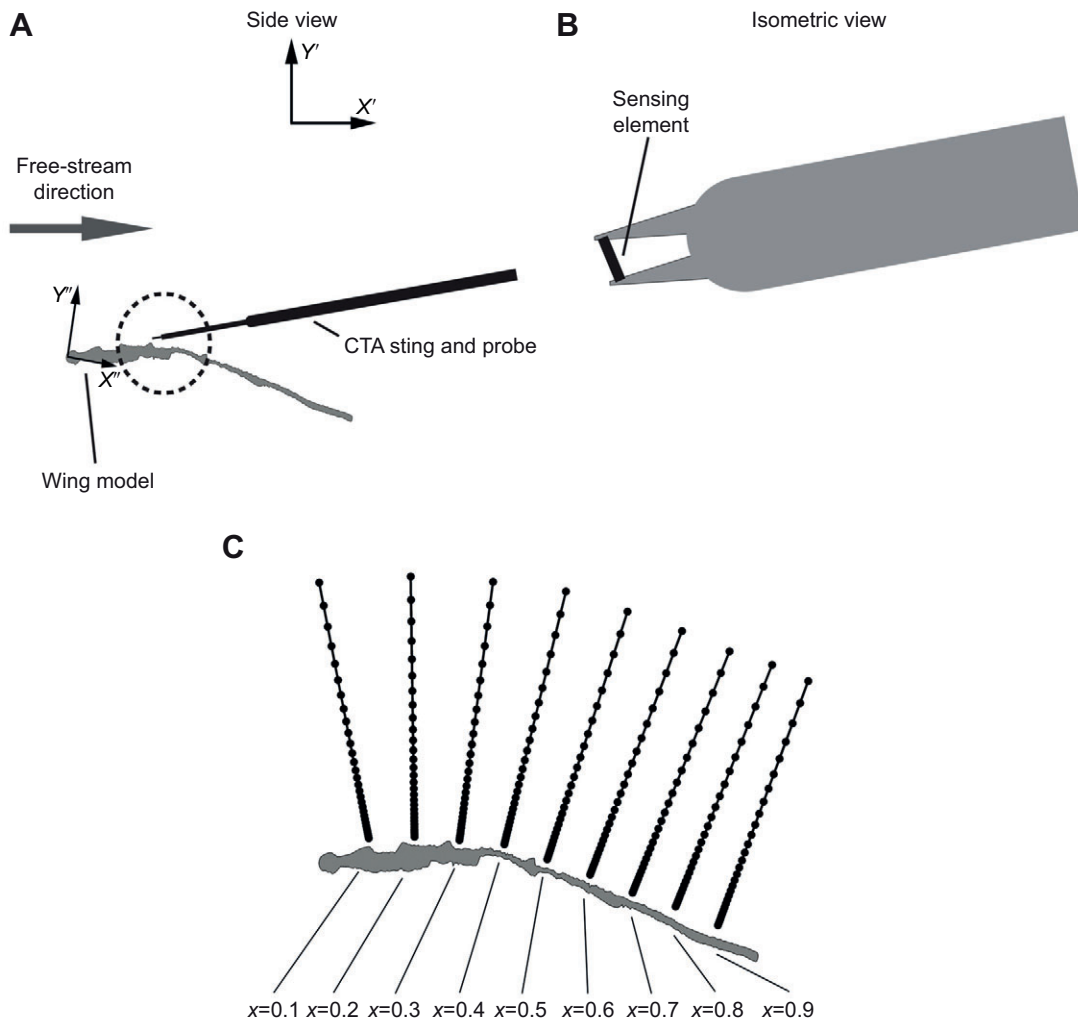


Fig. 3. (A) Schematic description of the constant-temperature anemometry (CTA) measurement setup; the CTA probe is connected to a sting that is mounted downstream to the wing and facing upstream. Magnification of the dashed region is shown in B. (B) Close-up of the CTA probe; the sensing element is mounted between two prongs that are connected to the probe's housing. (C) Close-up of the measurement points at nine chord stations at a dimensionless location along the span (z) of 0.5 and an angle of attack of 10 deg. The black circles present actual measurement points. The points of each chord station are laid on a straight ray that is normal to the local cross-sectional curvature.

Dimensionless velocities will be denoted by the respective lowercase letters; thus, $v=V/\bar{U}$, $u=U/\bar{U}$; it is understood that $\bar{u}=1$. Two coordinate systems were used (see Fig. 3A): (1) a global coordinate system (X' , Y' , Z'), which aligns with the wind tunnel, and (2) a local coordinate system (X'' , Y'' , Z''), where X'' is the distance along the chord, Z'' is positive towards the wing tip and Y'' complements a right-hand system. Y (or the word 'height') is used to imply the distance between a measurement point and the surface of the wing. x and y are the non-dimensional distance along the chord ($x=X''/c'$) and the non-dimensional height ($y=Y''/c'$), respectively, where $c'(Z'')$ is the chord length at each span location. The non-dimensional distance along the span is referenced to the wing length, $z=Z''/R$. The frequency f is referenced to \bar{U}/\bar{c} , where \bar{c} is the wing's mean aerodynamic chord ($=45$ mm). This dimensionless frequency is identified as the Strouhal number, $St_c=f\bar{c}/\bar{U}$.

The power spectral densities of the signals obtained within the boundary layer and the free stream are denoted by P_{vv} and P_{uu} , respectively. The power spectral density P_{vv} can be noisy; its integral, $C_{vv}(f)=[\int_0^f P_{vv}(f')df']^{1/2}$, is typically much smoother and allows easy assessment of the energy content at different frequency ranges. By

Parseval's theorem, $C_{vv}(\infty)=\sigma_v$, where σ_v is the standard deviation of v . Similarly, $C_{uu}(\infty)=\sigma_u$. A rapid increase of C_{vv} (or C_{uu}) with frequency is indicative of concentrated energy in a narrow spectral band.

The instantaneous velocity signals were acquired over the suction side of the wing model at five span locations (Fig. 1). In each span location, velocity profiles at nine chordwise stations were obtained, starting at 10% of the local chord and ending near the local trailing edge ($x=0.9$). Each velocity profile is reconstructed using 30 measurement points, starting from the vicinity of the wall (~ 1 to 1.5 mm from the physical wall) and marching further out in the direction normal to the wall. A representative example that shows the discrete measurement points is shown in Fig. 3C (for $z=0.5$). For clarity, the following figures do not denote explicitly the actual location of the measurement points.

As the CTA measurements over the entire wing lasted for hours, temperature compensation was applied to account for the temperature fluctuations that were associated with the wind tunnel facility (in addition to the fact that the environmental temperature was controlled).

Stereo particle image velocimetry

Larger fields of view were examined using an SPIV system from LaVision (Goettingen, Germany), which included two 120mJ Nd:YAG lasers, two 1376×1040 pixel resolution thermo-electrically cooled 12 bit Imager Intense CCD cameras and a programmable timing unit. A 50 mm cylindrical lens was used to create the light sheet in conjunction with a variable focal length lens (0.5 to 1.5 m) to focus the sheet at the measurement domain. The laser light sheet was aligned with the area of interest using a computer-controlled three axis traversing system mounted below the test section and the flow was seeded with water-based smoke particles with a typical diameter of 1 μm that were generated by a theatrical fog machine. The cameras were positioned to visualize the same field of view with an approximate 45 deg angular separation between their viewing angles. The focal issues associated with the angular misalignment were then compensated for with a Scheimpflug adapter (LaVision) mounted between each camera and its lens. A pair of 105 mm lenses was used to acquire SPIV data on the same planes in which CTA measurements were conducted. For each SPIV plane, the three velocity components were computed from the cross-correlation of pairs of successive images with 50% overlap between the interrogation domains. The images were processed using an advanced multi-pass method where the initial and final correlation passes were 32×32 and 16×16 pixels, respectively. Five hundred image pairs were acquired for the time-averaged measurements. The cameras were mounted at a perpendicular distance of ~1 m to the laser light. The free-stream velocity corresponds to an average displacement of ~8 pixels with an approximate error of ±0.2 pixels. This corresponds to a maximum measurement error of ±2.5% of the free-stream velocity.

RESULTS

Flow field at a Reynolds number of 5000

Time-averaged velocity profiles were generated for a Reynolds number of 5000 at five span locations for two angles of attack (Fig. 4). One-dimensional CTA measurements do not provide information about the flow direction; therefore, flow reversal could not be resolved. However, an inflection point along the velocity profile (see specific marking in Fig. 4) characterizes the formation of a shear layer (Michalke, 1965) downstream to a flow separation point, and acts as an indirect flow separation indicator. Using this indicator, it can be seen that the velocity profiles at an angle of attack of 0 deg represent an essentially attached flow field in the vicinity of the leading edge, although shallow and moderate flow separation regions were observed in some regions over the wing; for instance, inflectional velocity profiles can be seen in the vicinity of the wall at spanwise locations $z=0.3$ and 0.4 for $x>0.3$ (Fig. 4B,C for $\alpha'=0$ deg).

We quantify the boundary layer thickness as the height where the velocity profile experiences its maximal value instead of the conventional formulation, which suits boundary layers over flat plates (Schlichting and Gersten, 2000). This alternative was chosen because the common approximation of zero normal-to-the-surface pressure gradient is no longer valid over curved surfaces. Characteristic boundary layer thickness values vary from $0.1c'$ (for $\alpha'=0$ deg) to $0.2c'$ (or more) at an angle of attack of 10 deg, which illustrates the thick boundary layers that develop in this Reynolds number regime.

Another flow feature that characterizes thick boundary layers over airfoils is a reduced pressure recovery along the aft half of the airfoil's suction side; the monotonically thickening boundary layer along the local chord induces either a pressure decrease or

eliminates the pressure recovery that commonly characterizes airfoils at Reynolds numbers above 10^5 . This phenomenon causes enhanced suction along the majority of the chord, which contributes additional pressure drag. In the presented cases (for instance, see the framed region in Fig. 4A), this phenomenon originates from (1) a monotonically thickening boundary layer (like at $\alpha'=0$ deg) and (2) a separated flow region that does not reattach ($\alpha'=10$ deg). At $z=0.5$ and $z=0.7$ for an angle of attack of 10 deg (Fig. 4D,E), the formation of the shear layer is postponed to the aft half of the cross-section. We attribute this phenomenon to the lower local Reynolds number, $Re_c=Re_\infty c'/\bar{c}$, which stabilizes the flow field; low-velocity standard deviation values (Fig. 5C) strengthen this conclusion.

At an angle of attack of 10 deg and $z\leq 0.4$, the flow separation point is at approximately $x=0.3$, where \bar{v} suddenly dives towards zero. Similar to the results at $\alpha'=0$ deg, the separated flow region is characterized by the appearance of an inflection point along the velocity profile. Unlike free shear layers, the existence of the wing surface at the lower extent of the mixing layer translates to a boundary condition that differs from that of a free shear layer. Nevertheless, Rist and Maucher (Rist and Maucher, 2002) showed that the hydrodynamic stability characteristics of such velocity profiles resemble quite accurately those of free shear layers in cases where the height of the separation bubble is larger than 55% of the total boundary layer thickness. Indeed, the velocity profiles at an angle of attack of 10 deg satisfy this condition in most regions where a shear layer was identified.

Shear layers, which are commonly called mixing layers, are unstable to two-dimensional flow disturbances (Fjørtoft, 1950; Michalke, 1965; Rayleigh, 1880). They experience the maximal disturbance growth rate in the vicinity of the inflection point along the velocity profile. A look at the normalized velocity standard deviation against the time-averaged velocity profile (Fig. 5) shows that in all measured velocity profiles, the strongest velocity undulations were observed in the regions of maximal shear – in agreement with the amplification modes of mixing layers (Michalke, 1965). Nevertheless, it is interesting to note that the velocity standard deviation reaches ~30% of the free-stream velocity at a Reynolds number of 5000. *A posteriori*, these high values of velocity unsteadiness do not satisfy the main assumption of the mixing layer linear stability analysis. However, the distribution of the amplitude of flow unsteadiness across the boundary layer resembles the unsteady characteristics illustrated by the linear stability analysis of Michalke (Michalke, 1965).

The power spectral density of the velocity fluctuations within the boundary layer is shown in Fig. 6 at the height where they were maximal (these points are marked by black circles in Fig. 5) and the concurrent fluctuations of the free stream. The C_{vv} of the same cases is shown in Fig. 7; whereas P_{vv} is a direct measure of the velocity fluctuations energy, C_{vv} clearly shows cases where the velocity fluctuations cumulative energy follows that of the free stream. At the bounded region $z<0.5$ and $x\leq 0.3$ as well as at the wing's distal stations (along the entire chord), most of the undulation energy is concentrated at low frequencies, e.g. where $St_c<0.1$ (Fig. 7). Moreover, at these locations, the flow undulation spectra within the boundary layer and in the free stream are similar, only the amplitude of the former is larger by one or two orders of magnitude. This phenomenon is discussed below in detail (see Discussion, Low-frequency amplification). At $z<0.5$ along the aft half of the local chord (Fig. 7), a considerable part of the energy is concentrated at the medium frequencies, where $1<St_c<10$. These frequencies are associated with flow instabilities and, eventually, turbulence.

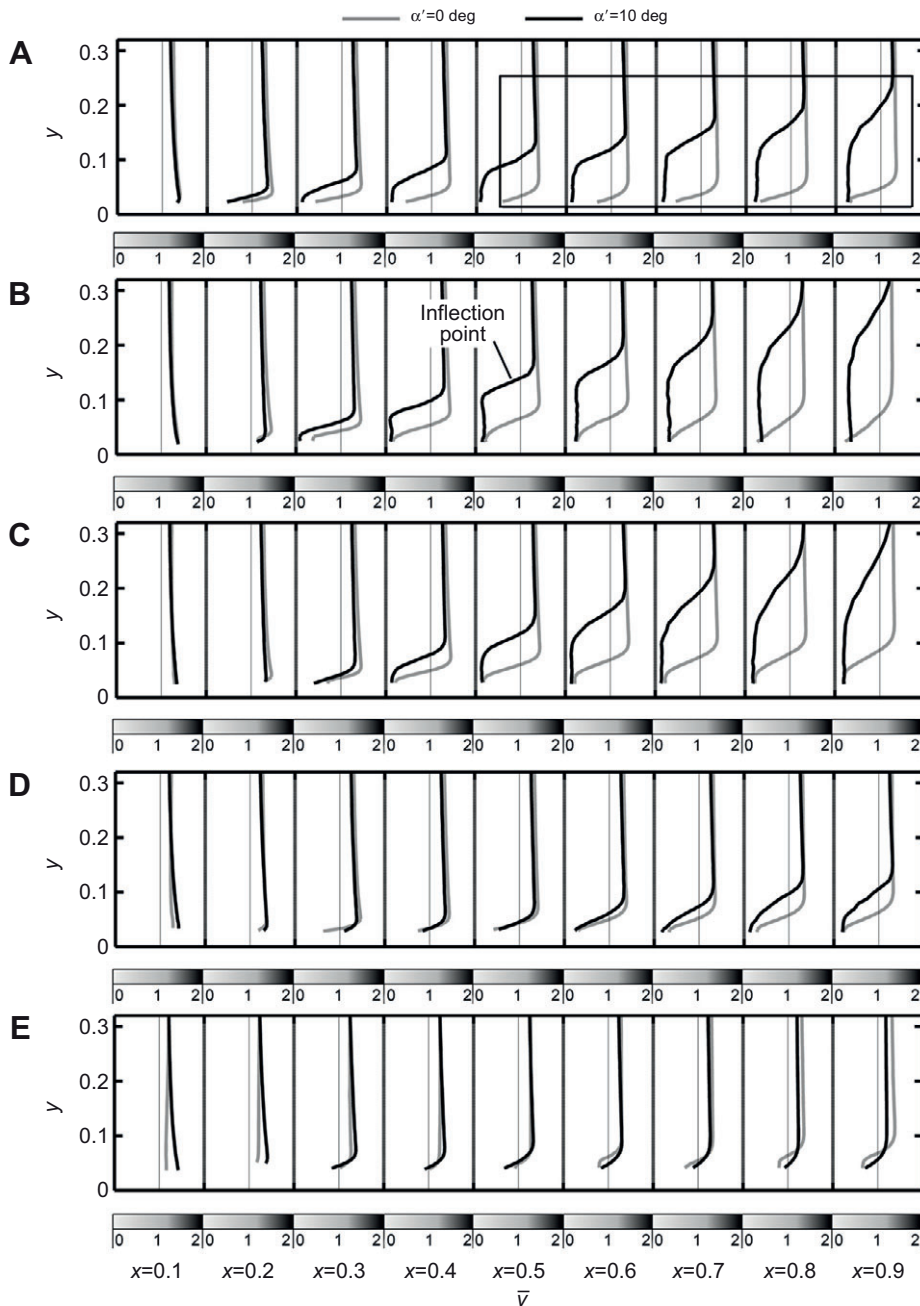


Fig. 4. Time-averaged velocity profiles at a Reynolds number of 5000 and two angles of attack, 0 deg (gray lines) and 10 deg (black lines). (A) $z=0.2$; (B) $z=0.3$; (C) $z=0.4$; (D) $z=0.5$; (E) $z=0.7$. The gray scale bars beneath each figure separate the results that were obtained at nine chord locations for each span station (x). Along each bar the dimensionless time-averaged velocity varies from 0 to 2.

Flow field at a Reynolds number of 10,000

Qualitatively, the velocity profiles obtained at Reynolds numbers of 5000 and 10,000 were similar. Therefore, another perspective of the velocity field will be provided by the SPIV results, which are characterized by higher spatial resolution. The velocity field resolved by SPIV lacks the high spectral resolution of the CTA technique, but it nevertheless resolves the different components of the velocity field instantaneously. Representative time-averaged velocity fields at different span locations are shown in Fig. 8. In this figure (time-averaged) streamlines are superimposed on the time-average of the instantaneous dimensionless spanwise vorticity field, $\hat{\omega}_z = \omega_z c / \bar{U}$, where ω_z is the dimensional spanwise vorticity field. The vorticity color map ranges from blue (clockwise vorticity) to red (counterclockwise vorticity). The time-averaged vorticity field at an angle of attack of 10 deg shows that the flow separates from the wing's suction side, in agreement with the CTA results. Downstream

to the flow separation point a mixing layer forms, as can be seen by the existence of a saturated clockwise vorticity band. In agreement with the CTA results, the mixing layer thickness increases along the local chord as a result of momentum diffusion. Although the leading-edge region was not illuminated during these tests, the time-averaged streamlines are indicative of a smooth surface separation, which indirectly suggests that no leading-edge vortex is present.

The 500 image pairs that were acquired at each spanwise location improved the signal-to-noise ratio of the time-averaged flow field; in addition, they provided statistical properties of flow field. Although such a record is not sufficient for proper spectral analysis, the velocity field standard deviation resolved by the SPIV analysis agrees with the CTA results (Fig. 9A). This fact demonstrates that the 500 image pairs are sufficient to resolve the turbulence intensity of the flow. To better understand the origin of these large velocity fluctuations, an instantaneous snapshot of the normalized vorticity

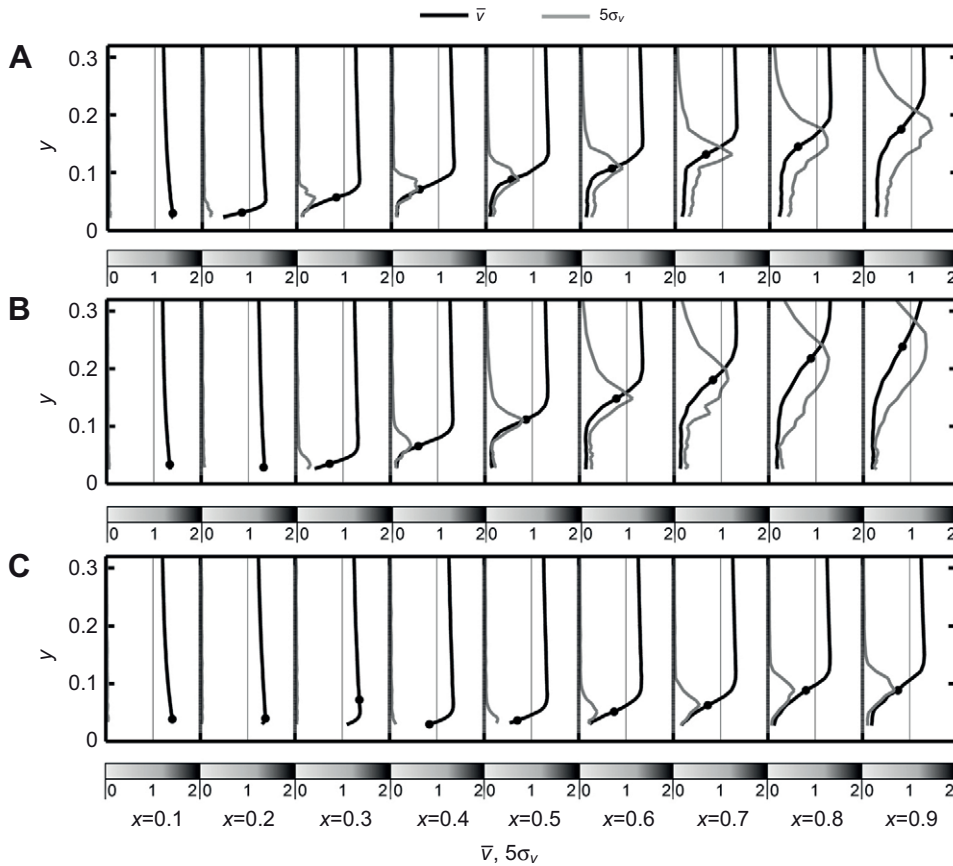


Fig. 5. Time-averaged velocity profiles (black lines) and velocity standard deviation distributions (gray lines) at a Reynolds number of 5000 and an angle of attack of 10 deg. Standard deviation values are magnified fivefold for clarity. (A) $z=0.2$; (B) $z=0.4$; (C) $z=0.5$. The gray scale bars beneath each figure separate the results that were obtained at nine chord locations for each span station (x). Along each bar the dimensionless time-averaged velocity varies from 0 to 2.

field is shown in Fig. 9B. The mixing layer, which develops at the upstream portion of the local chord, turns into a series of unsteady vorticity concentrations. These vorticity concentrations evolve from the mixing layer and shed downstream continuously. This unsteady flow state explains why both SPIV and CTA results resolve such high velocity fluctuations within the mixing layer.

In view of these results, it is worth emphasizing the difference between the time-averaged flow field (Fig. 8) and the instantaneous one (Fig. 9B); although the unsteady vorticity concentrations are formed and shed downstream, the time-averaged flow field does not adequately represent these coherent flow structures. Furthermore, these flow structures contribute to the transitional mixing and ultimately

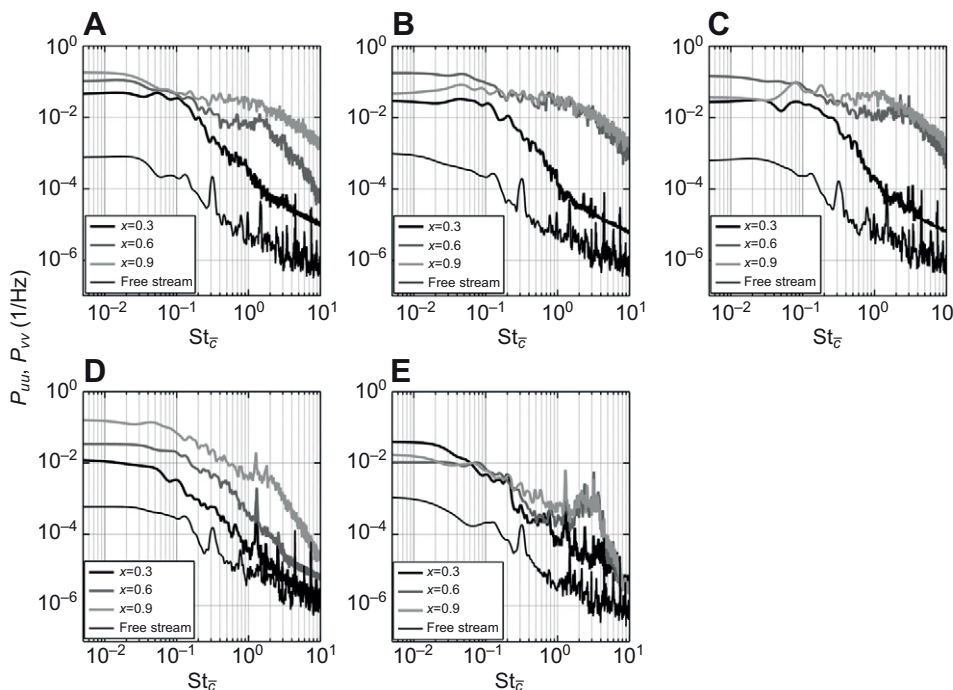


Fig. 6. Power spectral densities (for the dimensionless free-stream and boundary layer signals, P_{uu} and P_{vv} , respectively) of the velocity fluctuations at the height of maximal normalized velocity standard deviation. These heights are marked by black circles in Fig. 5. Conditions are the same as in Fig. 5. (A) $z=0.2$; (B) $z=0.3$; (C) $z=0.4$; (D) $z=0.5$; (E) $z=0.7$.

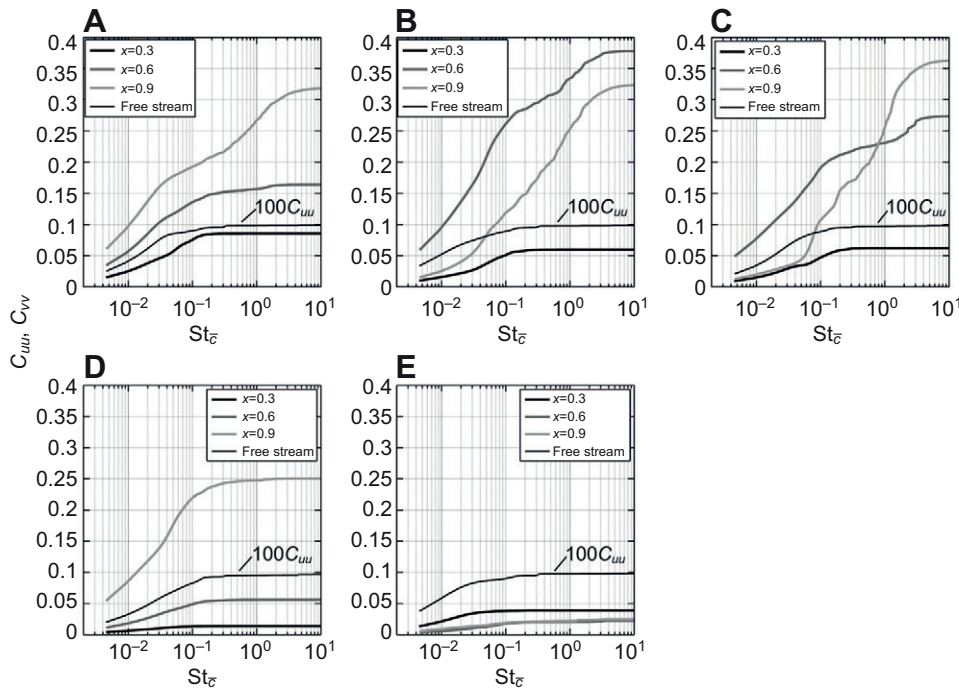


Fig. 7. Energy content (for the dimensionless free-stream and boundary layer signals, C_{uv} and C_{uu} , respectively) of the velocity fluctuations at the height of maximal normalized velocity standard deviation. To be visible in the figures, the free-stream values were magnified 100-fold. Conditions of the presented cases are the same as in Fig. 5. (A) $z=0.2$; (B) $z=0.3$; (C) $z=0.4$; (D) $z=0.5$; (E) $z=0.7$.

lead to the emergence of turbulent flow. Identification of these flow structures helps to illustrate how higher momentum is brought to the lower portions of the boundary layer, which contributes to the reattachment of the separation bubble. In this context, the time-averaged bubble geometry should be interpreted as an outcome of this transitional mixing mechanism.

Flow field at a Reynolds number of 15,000

At a Reynolds number of 15,000, the nature of the flow changes (e.g. Fig. 10); the velocity gradients in the vicinity of the wall become

non-zero. The inflection point diminishes and the velocity profile is characterized by decreasing values of maximal shear. This shows that the separation bubble reattaches in the time-averaged sense. Another example of this can be seen in Fig. 11C, where the flow reattaches at approximately $x=0.6$. Nevertheless, the flow undulation levels reach values of approximately $\sigma_v=0.4$ at $z=0.4$ (Fig. 11C). Under these flow conditions, the velocity undulations are considerable throughout the wing length. The spectral analysis shows that the velocity fluctuation spectrum is wide and reaches St_c of ~ 10 (Fig. 12). At all span stations the energy of the velocity

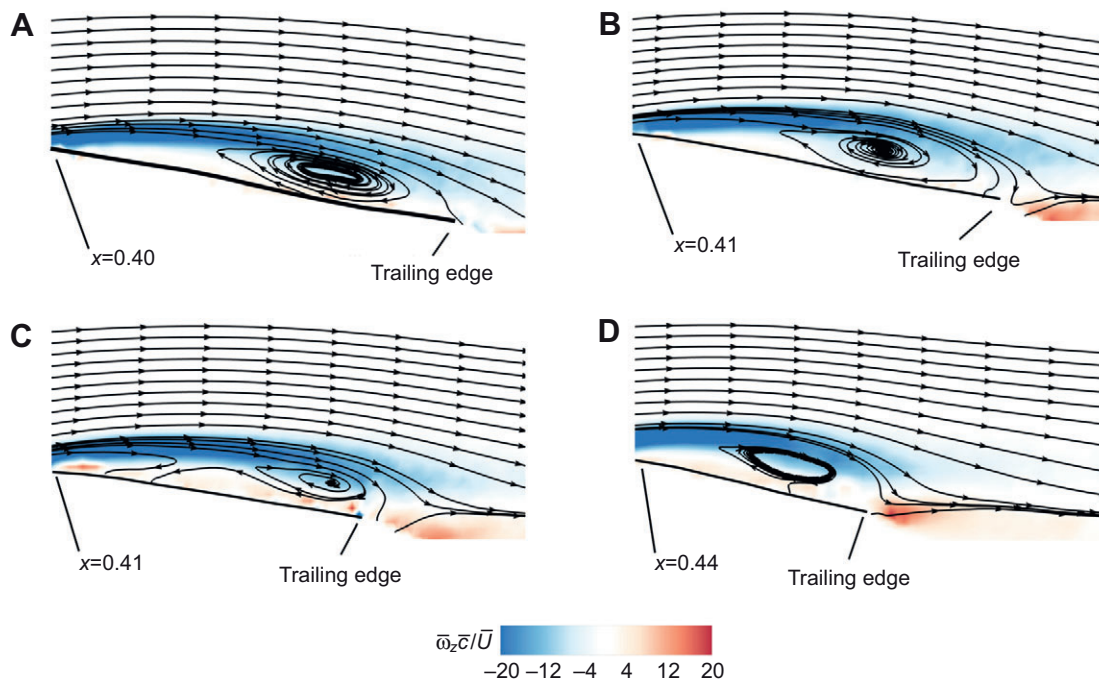


Fig. 8. Contours of time-averaged spanwise vorticity and streamlines as resolved by stereo particle image velocimetry (SPIV) at a Reynolds number of 10,000 and an angle of attack of 10 deg. (A) $z=0.3$; (B) $z=0.4$; (C) $z=0.5$; (D) $z=0.7$. The color scale indicates time-averaged spanwise vorticity from blue (clockwise vorticity) to red (counterclockwise vorticity).

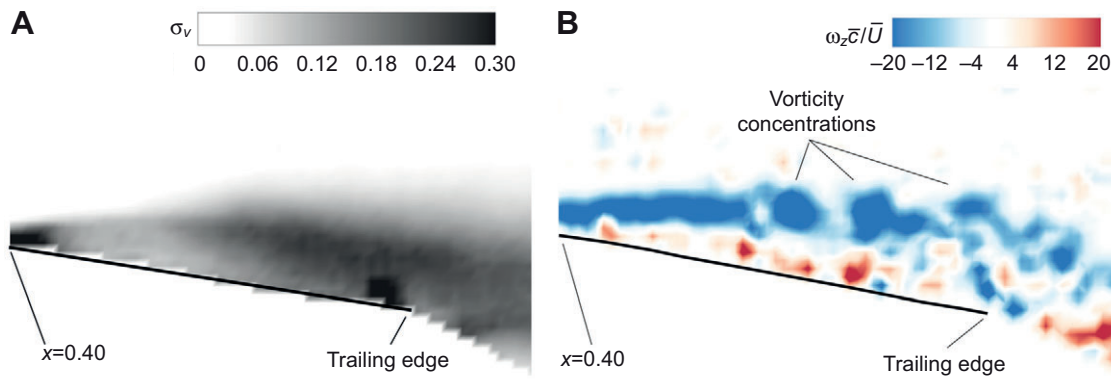


Fig. 9. SPIV results obtained at the same conditions as in Fig. 8, $z=0.4$. (A) Contours of the dimensionless velocity standard deviation. (B) Contours of instantaneous spanwise vorticity.

fluctuations extends beyond the spectrum of the free-stream velocity fluctuations. It is noteworthy that the amplitude of the velocity fluctuations decays along the local chord at spanwise stations $z=0.2$ and $z=0.4$ (Fig. 12A,C). This phenomenon can be explained by the fact that the time-averaged velocity profiles in these span stations are no longer inflectional (Fig. 11A,C); this leads to a decay of the flow disturbances amplitude (or, alternatively, a partial laminarization). Moreover, this phenomenon demonstrates that the mixing layer is the dominant flow mechanism involved in the laminar-to-turbulent transition process.

To elucidate the aerodynamic effect of flow reattachment, velocity signals were acquired in the near wake (5 mm downstream of the wing's trailing edge) at two span locations where flow reattachment was apparent. The time-averaged velocity profiles and their respective standard deviations are given for two Reynolds numbers in the Appendix (Fig. A3). It is a common practice to evaluate the cross-sectional drag coefficients by calculating the net momentum change in a control volume that contains the wing's cross-section (Schlichting and Gersten, 2000). However, the net force that acts on the outer boundary of such a control volume approaches zero only when the static pressure within the wake reaches asymptotically the free-stream value. In such cases, the cross-sectional drag coefficient can be evaluated using the free stream and the velocity distribution across the wake. Therefore, the current near-wake velocity profile cannot yield the cross-sectional drag coefficient. Nevertheless, it is apparent that the momentum deficit at a Reynolds number of 15,000 is considerably lower than that at a Reynolds number of 5000, which reflects the aerodynamic effect of the separation bubble reattachment.

DISCUSSION

Emergence of turbulent flow

In order to visualize the evolution of the emerging turbulent flow field, the maximal velocity standard deviation is shown on top of the wing planform for three Reynolds numbers (Fig. 13). At each span station, the velocity signals were acquired at points that form a ray-like pattern (one ray per chord station), as depicted in Fig. 3C. Each ray is represented in Fig. 13 by a black circular symbol, plotted at the projection of the first measurement point along the ray (in the vicinity of the surface). Therefore, Fig. 13 presents the values of maximal velocity standard deviation acquired at each ray.

At an angle of attack of 0 deg (Fig. 13A–C), the maximal velocity standard deviation is non-zero at the medial portions of the wing. A correlation between the velocity undulation contours and the feather texture is apparent. Although the feather shafts cause local flow separation and some level of unsteady flow, the velocity standard

deviation σ_v is less than 0.2. As shown above, these flow mechanisms are insufficient to enhance the mixing to a level that may lead (in the time-averaged sense) to reattachment of the separation bubble.

Hummingbirds, however, operate at higher angles of attack. An angle of attack of 10 deg represents a case of higher biological relevance. At this angle of attack the velocity standard deviation depicts a distinct difference between the inbound and outbound portions of the wing (Fig. 13D–F): the turbulence levels are considerably higher near the wing root, even at a Reynolds number of 5000. As detailed above, the high-velocity undulation levels are not in the vicinity of the wing surface (Figs 5, 11). Therefore, the rough texture that characterizes the wing root region (contributed by the coverts) is unlikely to promote transition in operational conditions. The adverse pressure gradient that is derived from the local cross-sectional camber and the angle of attack of the wing promotes separation and formation of a mixing layer. This mechanism leads to high levels of flow undulations, enhance mixing and, eventually, turbulence. At the distal portions of the wing, where the local cross-sectional camber and leading edge radius diminish, a distinct change of the unsteady flow characteristics is observed only at a Reynolds number that is somewhat above 10,000.

At a Reynolds number of 15,000, high-velocity standard deviation was not restricted to the medial portion of the wing; as matter of

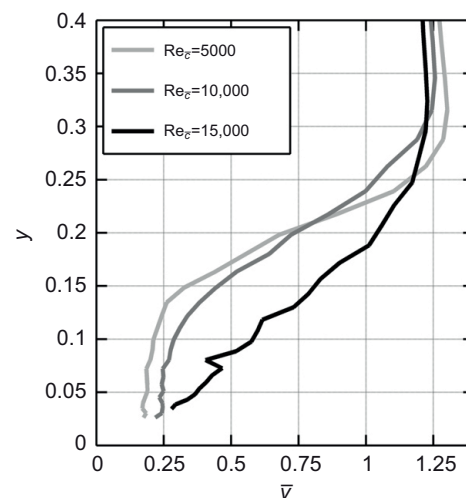


Fig. 10. Time-averaged velocity profiles acquired at three Reynolds numbers and at an angle of attack of 10 deg ($z=0.4$, $x=0.8$). In this example, the velocity profile at a Reynolds number of 15,000 has a non-zero gradient in the vicinity of the wing surface.

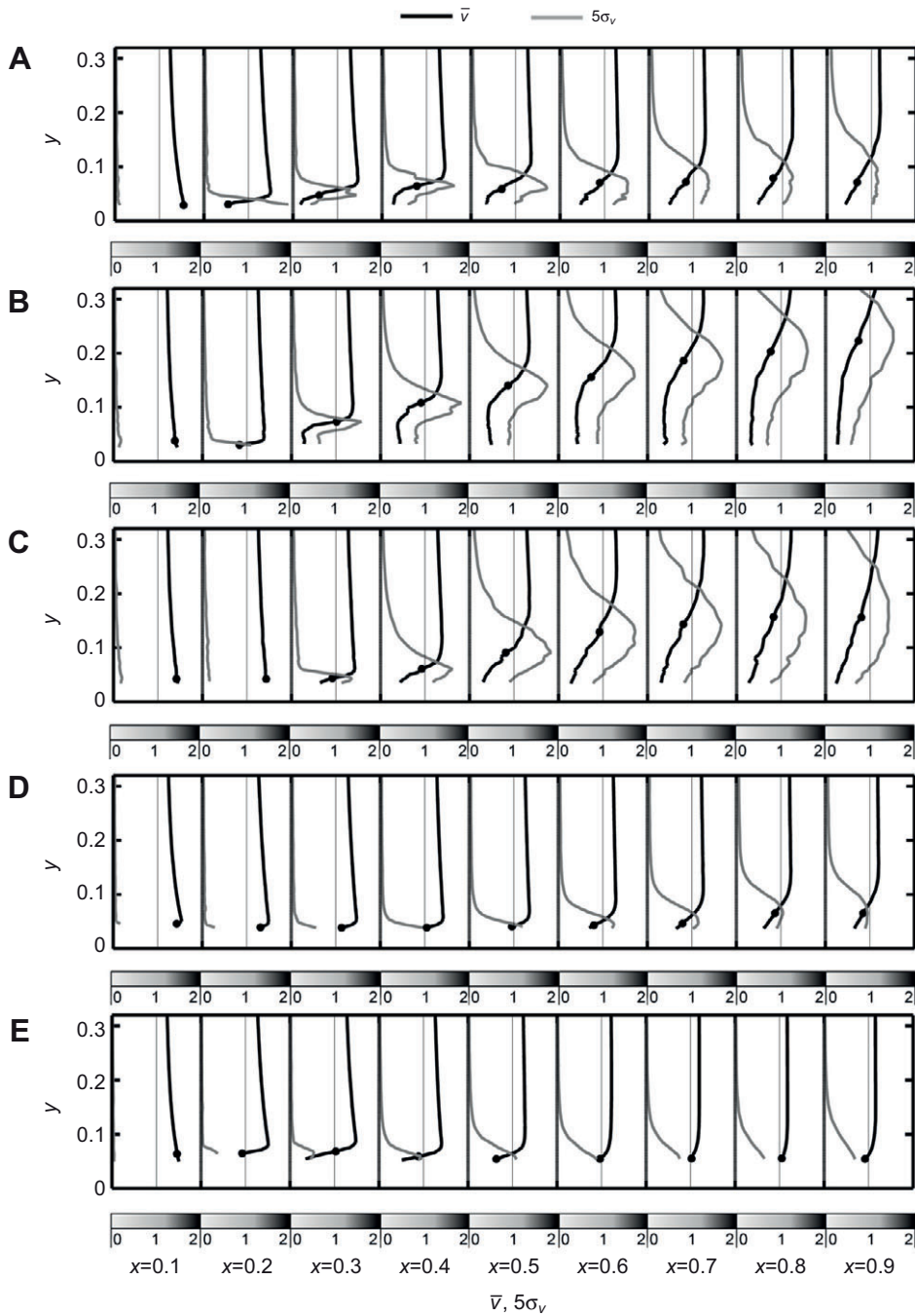


Fig. 11. Time-averaged velocity profiles (black lines) and velocity standard deviation distributions (gray lines) at a Reynolds number of 15,000 and an angle of attack of 10 deg. (A) $z=0.2$; (B) $z=0.3$; (C) $z=0.4$; (D) $z=0.5$; (E) $z=0.7$. The gray scale bars beneath each figure separate the results that were obtained at nine chord locations for each span station (x). Along each bar the dimensionless time-averaged velocity varies from 0 to 2.

fact, in the distal portion of the wing ($z \geq 0.4$), similar levels of velocity standard deviation were measured in the vicinity of the wing's leading edge (Fig. 13F). These observations led us to conclude that the primary 10th feather, which constructs the wing's leading edge at $z \geq 0.4$, has an aerodynamic effect but is effective only at Reynolds numbers that are high enough.

Growth rate

The experimental results showed that the flow disturbance amplitudes were intensifying along the chord (see Figs 6, 7). The intensification (or what is commonly called the growth rate of a flow disturbance) along the chord is quantified below and given for a few span locations. We define growth rate as $A(x, z^*)/A(x_0, z^*)$, where $A(x, z^*)$ is the amplitude of the flow disturbance $A(x, z^*)\text{Re}[e^{i(kx - 2\pi ft)}]$, where k is the (generally complex) wave

number and f is the frequency. x_0 is a reference location along the chord at a specific span location z^* and $A(x_0, z^*)$ is the flow disturbance amplitude in that location (i.e. the respective flow disturbance reference amplitude). The fact that inflectional velocity profiles were obtained from $x=0.3$ (see Figs 4, 5) led us to choose $x_0=0.3$ as a reference point in the following analysis. The growth rate that was obtained from the experimental results will be compared with the results of a simplified theoretical analysis for the same flow disturbance frequencies. Such a comparison will help us to identify the state of the actual flow mechanisms for given free-stream conditions (i.e. angle of attack and Reynolds number). In case the actual growth rates are of the same order of magnitude as those that were obtained theoretically, one may make indirect conclusions about the state of the measured velocity field. However, once the actual growth rates are much higher than those of the

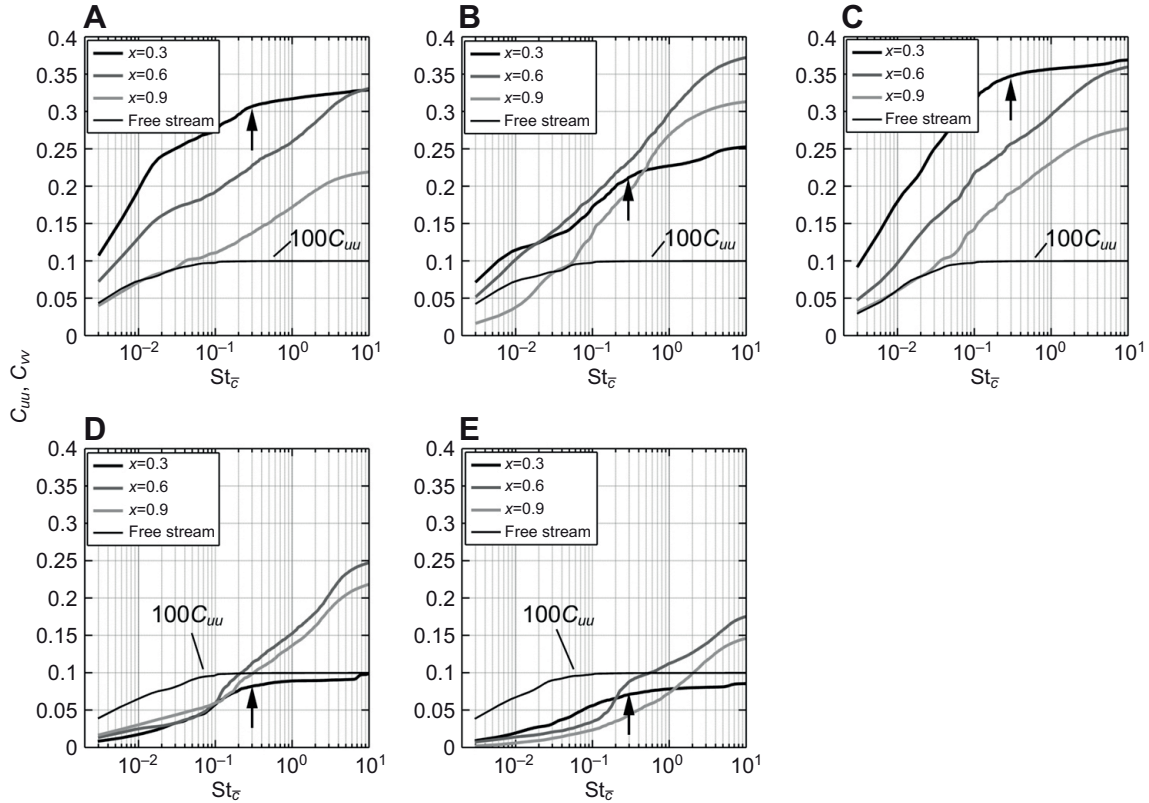


Fig. 12. C_{vv} and C_{uu} of the velocity fluctuations at the height of maximal normalized velocity standard deviation. These heights are marked by black circles in Fig. 11. To be visible in the figures, the free-stream values were magnified 100-fold. Conditions are the same as in Fig. 11. (A) $z=0.2$; (B) $z=0.3$; (C) $z=0.4$; (D) $z=0.5$; (E) $z=0.7$. The black arrows indicate C_{vv} values at $x=0.3$ for $St_c=0.3$.

theoretical model predictions, one can infer that the actual flow mechanisms are further developed and that the actual flow field does not satisfy the basic assumptions of the theoretical analysis.

Velocity profiles that were obtained at a Reynolds number of 5000 and an angle of attack of 10 deg (Fig. 4) have been curve-fitted (see Appendix, Fig. A1) using the following equation:

$$\bar{v} = \bar{v}_1 + \frac{\Delta\bar{v}}{2} \left(1 + \tanh \frac{2(y - y_s)}{\delta_s} \right), \quad (1)$$

where \bar{v}_1 is the velocity at the bottom of the separation bubble, $\Delta\bar{v}$ is the velocity jump across the shear layer, δ_s is a measure of the shear layer thickness and y_s is the height of maximal shear above the wing surface (velocities are normalized by the free-stream velocity; δ_s and y_s are referenced to the local chord length, c'). This model (Eqn 1) was chosen in order to implement a simple (inviscid) stability analysis (Michalke, 1965). Variation of these parameters along the chord is shown in the Appendix (Fig. A2). We will focus our analysis on the first three medial span locations because the shear layer in these locations was thick enough to be resolved properly. Application of an inviscid stability analysis for flows with separation was justified by Rist and Maucher (Rist and Maucher, 2002) for those cases where the height of the separation bubble is more than half of the total boundary layer thickness. Furthermore, Michalke's (Michalke, 1965) analysis was formulated for a shear layer of constant parameters (i.e. with no downstream dependence); because some of the parameters do vary (Fig. A2), only an upper bound of the flow disturbance growth rate will be evaluated below. Following Michalke, we assume a velocity disturbance of:

$$w(t, x, y) = \text{Re}[\hat{w}(y)e^{i(kx - 2\pi ft)}], \quad (2)$$

superimposed on the average velocity profile $\bar{v}(y) = (\Delta\bar{v}/2)[1 + \tanh(2y/\delta_s)]$. Adjusting the present notation to align with that of Michalke, we obtain $\alpha = k\delta_s/2$ and $\beta = \pi St_c \delta_s (c'/\bar{c})/\Delta\bar{v}$. The rationale is to compare the experimentally resolved growth rates with the theoretical (maximal) growth rates of two-dimensional flow disturbances with the same Strouhal numbers. The growth rate of two exemplary Strouhal numbers, $St_c=0.3$ and 1.1, is presented in Fig. 14. The former Strouhal number characterizes the wind tunnel facility; free-stream fluctuating energy beyond this Strouhal number was measured to be practically zero (Figs 7, 12). The latter Strouhal number characterizes a time scale of aerodynamic importance, as it is associated with the wing's mean aerodynamic chord and the free-stream velocity. The theoretical and experimental growth rates for the lower Strouhal number are of the same order of magnitude. However, the experimentally resolved growth rates for $St_c=1.1$ are much higher than the theoretical bounds. Such a rapid growth along the chord has to do with three-dimensional, rather than two-dimensional, flow disturbances. This conclusion agrees with the study of Rodríguez and Theofilis (Rodríguez and Theofilis, 2010). Whatever the form of disturbance, the most amplified flow disturbances within the boundary layer are in the frequency range of $St_c < 10$ (see the spectra in Fig. 6).

Low-frequency amplification

Velocity fluctuations at the forward half of the local chord (for $z \leq 0.4$) have standard deviations of up to $0.1V$ (100 times that of the free stream) and their energy is concentrated in the low-frequency band of the spectrum, i.e. below $St_c=0.3$ (Figs 6, 7). Moreover, the energy content of these velocity signals, C_{vv} , is similar in shape to that of the free stream, C_{uu} (Fig. 7A–C, $x=0.3$).

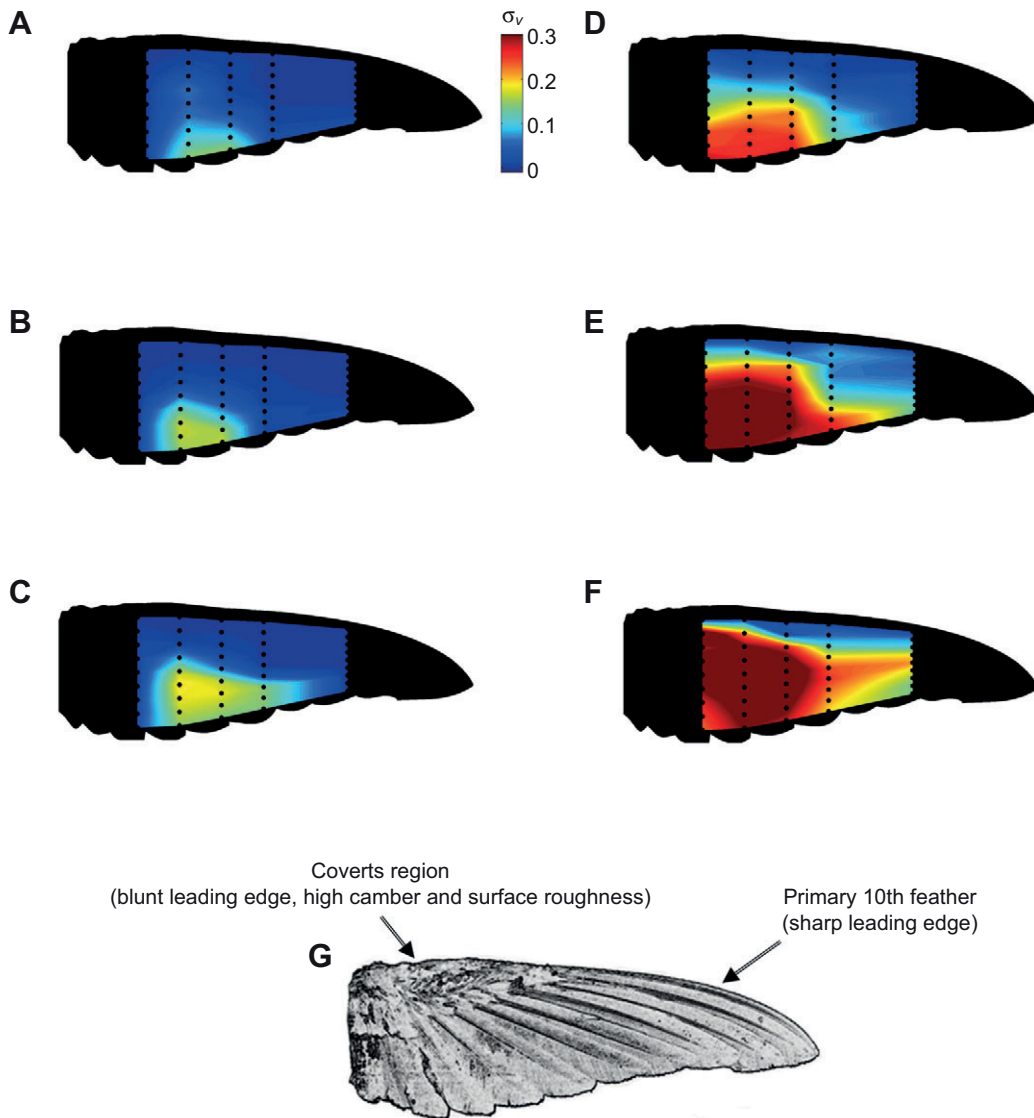


Fig. 13. Contours of maximal velocity standard deviation at angles of attack of 0 deg (A–C) and 10 deg (D–F). (A,D) $Re_c=5000$; (B,E) $Re_c=10,000$; (C,F) $Re_c=15,000$. (G) Wing texture, showing the bone region (which is covered by the coverts) and the feathers connected to it.

There is no convective instability mechanism within the boundary layer over the wing that can amplify velocity disturbances at the forward part of the local chord by two orders of magnitude. We believe that this amplification has to do with the response of the large vorticity concentrations (i.e. those of large wavelength) to free-stream disturbances. In fact, the characteristic time scale associated with a flow structure that is comparable in size to the mean aerodynamic chord is the time it takes the flow to cross this characteristic length scale, i.e. \bar{c}/\bar{U} . Such a flow structure will probably not respond to disturbances having a shorter time scale, but it should respond to disturbances of the free stream having a longer time scale, in particular those for which St_c is smaller than 0.3.

The response of the boundary layer in the vicinity of the leading edge (e.g. $x \leq 0.3$) to flow disturbances is manifested in variations of its thickness. Because the CTA measurements have been carried out at constant heights above the surface of the wing, small changes in the thickness of the boundary layer profile yield large changes in the total velocity (Fig. 15), especially if the measurement is taken near the point of maximal shear.

The observation that the variation between the minimal and maximal velocity profiles can be described as almost constant

vertical shift (marked as Δ_y) supports the argument that small changes in the boundary layer thickness are the origin of this velocity variation (Δ_v) and not a convective flow mechanism. A suggested mechanism that results in variation in boundary layer thickness is described below.

At a Reynolds number of 15,000 and an angle of attack of 10deg, the energy content of the low-frequency disturbances ($St_c \leq 0.3$) along the upstream medial portions of the wing was found to be approximately threefold higher than that which was measured at the outer span stations; to demonstrate this, one should compare C_{vv} values for $x=0.3$, $z \leq 0.4$ (Fig. 12A–C, black arrows) with the concurrent values measured at $z=0.5$ and 0.7 (Fig. 12D,E, black arrows). The fact that the maximal velocity gradients within the mixing layer were measured to be practically uniform across the wing span led us to associate the non-uniform low-frequency amplification with variations of the boundary layer thickness. As we see it, the only mechanism that can alter the boundary layer thickness is an unsteady movement of the flow separation location. In this context, smooth surface separation is more susceptible to flow disturbances whereas over a sharp leading edge the separation point is somewhat more robust. Indeed, the energy content of low-frequency flow disturbances

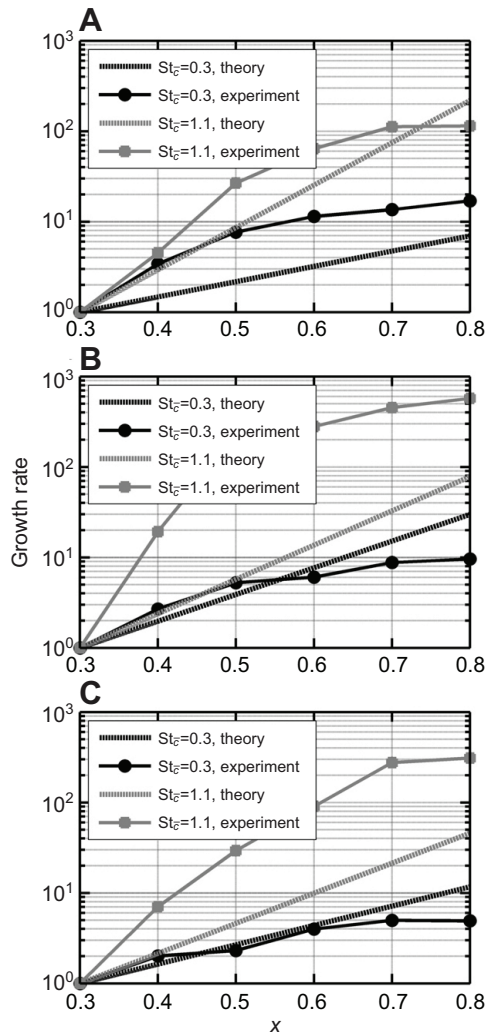


Fig. 14. Comparison between the measured flow disturbance growth rates (experiment) and the maximal growth rates predicted by the two-dimensional inviscid analysis (theory) for a Reynolds number of 5000 and an angle of attack of 10 deg. (A) $z=0.2$; (B) $z=0.3$; (C) $z=0.4$.

is positively correlated with the leading-edge radius along the span. In order to draw a more definite conclusion on this aspect, a dedicated setup of higher spatial resolution is required, especially in the vicinity of the leading edge.

Conclusions

High-fidelity measurements using CTA and SPIV allowed quantitative analysis of the flow field in the vicinity of a hummingbird wing model at chord-based Reynolds numbers that ranged from 5000 to 15,000. The transition process initiates at a Reynolds number as low as 5000. At a Reynolds number of 15,000, the turbulent mixing is capable of reattaching the separation bubble – a phenomenon of aerodynamic importance. The analysis concludes that the flow mechanisms over hummingbirds' wings in rectilinear flight cannot be considered as laminar. Instead, the flow field consists of a continuous spectrum of temporal and spatial scales that characterizes transitional and turbulent flows. The flow mechanism that triggers turbulence is a shear layer that evolves above the wing surface and not the rough texture of the wing surface. The primary 10th feather (i.e. the sharp leading edge)

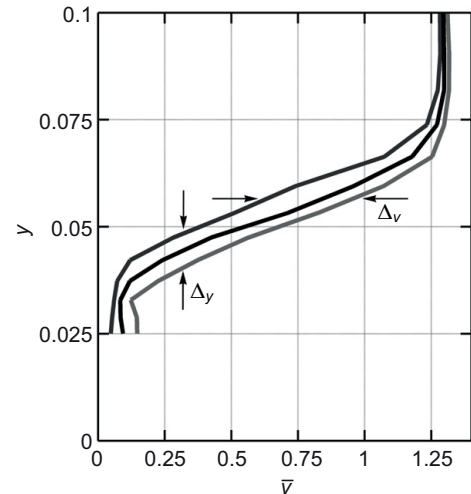


Fig. 15. Minimal (upper line), time-averaged (middle line) and maximal (lower line) velocity profiles at $z=0.3$ and $x=0.3$, obtained at a Reynolds number of 5000 and an angle of attack of 10 deg. Boundary layer dimensionless velocity variation is denoted by Δ_v ; Δ_y marks the boundary layer thickness variation.

affected the transitional process at Reynolds numbers somewhat greater than 10,000; furthermore, along the distal portion of the wing, the primary 10th feather was found to decrease the sensitivity of the flow separation point to free-stream disturbances (of low frequencies).

As such an in-depth analysis of the velocity field over a hummingbird wing model is not reported elsewhere, we hope that these insights will allow better understanding of the laminar-to-turbulent transition process that evolves over revolving and flapping wings operating in this Reynolds number regime.

APPENDIX

Additional experimental results

The velocity profiles and the results of their curve-fitting process are shown in Fig. A1 using Eqn 1 as the model. The model parameters, \bar{v}_1 , $\Delta\bar{v}$, y_s and δ_s , are functions of the dimensionless location along the local chord, x . Using a least-square curve-fitting technique that is implemented in MATLAB (such as `lsqcurvefit`), the model parameters are calculated along the chord for each span location. The curve-fitted model is presented on top of the experimental results in Fig. A1 (panels A, B, E and F), denoted by the thin solid black lines; the filled symbols denote the height of maximal shear, y_s . Panels C, D, G and H of the same figure demonstrate how the relevant velocity profiles in each span station collapse when the velocity profiles are presented using the dimensionless location within the shear layer, $2(y-y_s)/\delta_s$. The variation of the model parameters is shown in Fig. A2. One can see that the shear layer thickness, δ_s , does not vary considerably up to an x of 0.6 (although it does so further downstream), whereas the dimensionless velocity jump across the shear layer varies moderately. Both the location of maximal shear, y_s , and the minimal velocity in the vicinity of the wall, \bar{v}_1 , vary monotonically along the chord.

Time-averaged velocity profiles and velocity standard deviation distributions across the near wake of the wing are shown in Fig. A3 for two Reynolds numbers ($Re_c=5000$ and 15,000) at an angle of attack of 10 deg. The time-averaged velocity profiles present the momentum deficit in the near wake. The results at a Reynolds

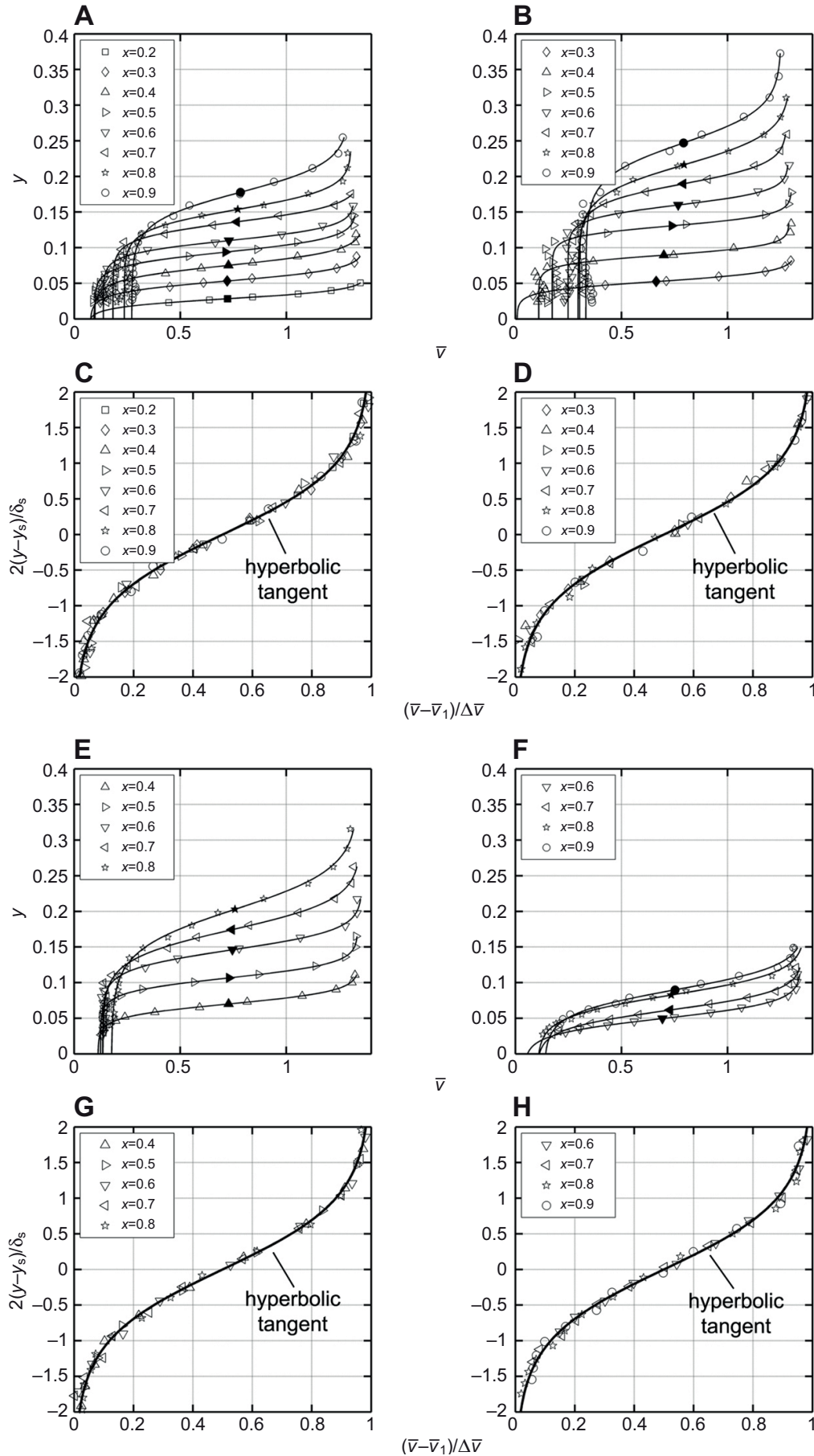


Fig. A1. Curve-fitting results. (A,B,E,F) Time-averaged velocity profiles and their respective curve-fit. (C,D,G,H) Self-similar representation of the time-averaged velocity profiles. The solid black lines illustrate the model (Eqn 1), for reference. (A,C) $z=0.2$; (B,D) $z=0.3$; (E,G) $z=0.4$; (F,H) $z=0.5$.

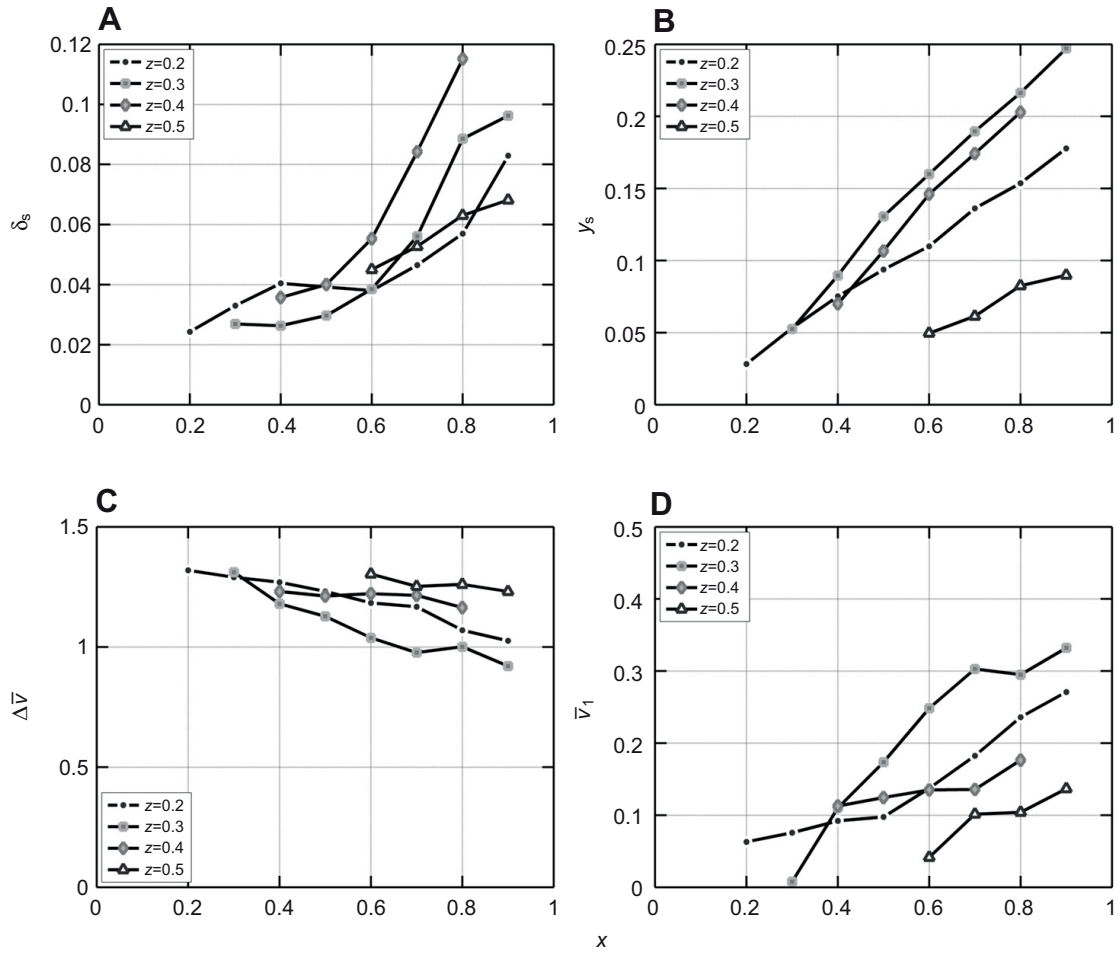


Fig. A2. Parameters of the hyperbolic-tangent fit. (A) Shear-layer representative length scale; (B) height of maximal shear; (C) velocity jump across the shear-layer; and (D) velocity at the bottom of the separation bubble.

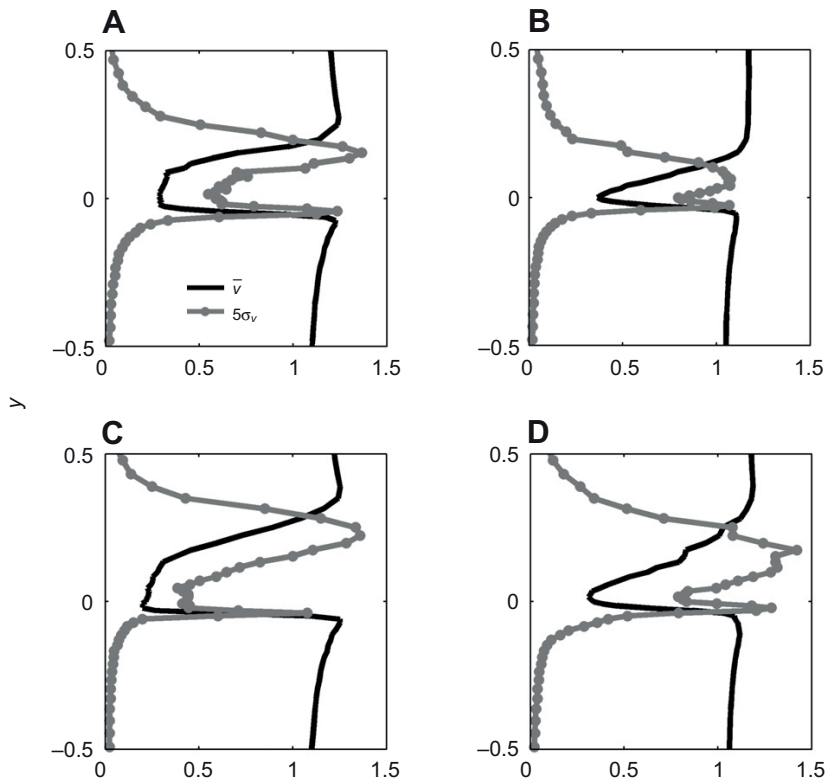


Fig. A3. Time-averaged velocity profiles (black lines) and velocity standard deviation distributions (gray lines) across the near wake of the wing at an angle of attack of 10 deg. (A,C) $Re_c=5000$; (B,D) $Re_c=15,000$. (A,B) $z=0.2$; (C,D) $z=0.4$.

number of 15,000 (Fig. A3B,D) show a considerably lower momentum deficit than that which was obtained at a Reynolds number of 5000 (Fig. A3A,C).

LIST OF SYMBOLS AND ABBREVIATIONS

δ	flow disturbance amplitude
\bar{c}	mean aerodynamic chord
c'	local chord length
CTA	constant-temperature anemometry
C_{uu}	energy content of the dimensionless free-stream signal
C_{vv}	energy content of the dimensionless total velocity signal
D	aerodynamic drag
f	frequency
k	wavelength
L	aerodynamic lift
P_{uu}	power spectral density of the dimensionless free-stream signal
P_{vv}	power spectral density of the dimensionless total velocity signal
R	wing length
Re_c	Reynolds number based on mean aerodynamic chord
$Re_{c'}$	Reynolds number based on local chord length
SEM	scanning electron microscopy
SPIV	stereo particle image velocimetry
St_c	dimensionless frequency, Strouhal number
t	time
u	dimensionless free-stream velocity
\bar{u}	time-averaged dimensionless free-stream velocity
u'	velocity component in the X' direction
U	free-stream velocity
\bar{U}	time-averaged free-stream velocity
v	dimensionless total velocity in a streamwise plane
\bar{v}	time-averaged dimensionless total velocity in a streamwise plane
\bar{v}_1	dimensionless total velocity at the bottom of the shear layer (time-averaged)
V	total velocity in a streamwise plane
x	dimensionless location along the local chord
x_0	reference chord station
(X', Y', Z')	wind-tunnel coordinate system
(X'', Y'', Z'')	wing coordinate system
y	dimensionless height above the wing surface
Y	height above the wing surface
y_s	height of maximal shear
z	dimensionless location along the span
α'	geometric angle of attack
δ_s	shear layer width
Δ_v	boundary layer dimensionless velocity variation
$\Delta\bar{v}$	dimensionless total velocity jump across the shear layer (time-averaged)
Δ_y	boundary layer thickness variation
σ_u	standard deviation of the free-stream velocity
σ_v	standard deviation of the velocity within the boundary layer
ω_z	instantaneous spanwise vorticity
$\hat{\omega}_z$	dimensionless spanwise vorticity

ACKNOWLEDGEMENTS

Y.E. is grateful to Prof. Michael Amitay, who lent the SPIV system during the experiments. We thank Dr Douglas Altshuler for providing specimens of *Calypte anna* wings.

FUNDING

Y.E. was supported in part by the Joan and Reginald Coleman-Cohen Fund.

REFERENCES

- Altshuler, D. L., Dudley, R. and Ellington, C. P. (2004). Aerodynamic forces of revolving hummingbird wings and wing models. *J. Zool.* **264**, 327-332.
- Bennett, L. (1966). Insect aerodynamics: vertical sustaining force in near-hovering flight. *Science* **152**, 1263-1266.
- Bomphrey, R. J., Lawson, N. J., Harding, N. J., Taylor, G. K. and Thomas, A. L. R. (2005). The aerodynamics of *Manduca sexta*: digital particle image velocimetry analysis of the leading-edge vortex. *J. Exp. Biol.* **208**, 1079-1094.
- Bruun, H. H. (1996). Hot-wire anemometry: principles and signal analysis. *Meas. Sci. Technol.* **7**, doi.org/10.1088/0957-0233/7/10/024.
- Edmonds, V. L. (2005). Gliding flight in megabats. PhD thesis, Cambridge University, Cambridge, UK.
- Elimelech, Y. (2010). Flow fields over airfoils at Reynolds numbers between 5000 and 50000. PhD thesis, Technion – Israel Institute of Technology, Haifa, Israel.
- Ellington, C. P. (1984). The aerodynamics of hovering insect flight. I. The quasi-steady analysis. *Philos. Trans. R. Soc. Lond. B* **305**, 1-15.
- Ellington, C. P. (2006). Insects versus birds: the great divide. AIAA paper 2006-35. In *Proceedings of the 44th AIAA Aerospace Sciences Meeting and Exhibit*. Reston, VA: AIAA.
- Ellington, C. P. and Usherwood, J. R. (2001). Lift and drag characteristics of rotary and flapping wings. In *Fixed and Flapping Wing Aerodynamics for Micro Air Vehicle Applications* (ed. T. Mueller), pp. 231-248. Reston, VA: Progress in Aeronautics and Astronautics.
- Ellington, C. P., Van den Berg, C., Willmott, A. P. and Thomas, A. L. R. (1996). Leading-edge vortices in insect flight. *Nature* **384**, 626-630.
- Fjørtoft, R. (1950). Application of integral theorems in deriving criteria for stability for laminar flows and for baroclinic circular vortex. *Geophys. Publ.* **17**, 1-52.
- Lentink, D. and Dickinson, M. H. (2009). Rotational accelerations stabilize leading edge vortices on revolving fly wings. *J. Exp. Biol.* **212**, 2705-2719.
- Maxworthy, T. (1979). Experiments on the Weis-Fogh mechanism of lift generation by insects in hovering flight. Part 1. Dynamics of the 'filing'. *J. Fluid Mech.* **93**, 47-63.
- Maxworthy, T. (1981). The fluid dynamics of insect flight. *Annu. Rev. Fluid Mech.* **13**, 329-350.
- Maxworthy, T. (2007). The formation and maintenance of a leading-edge vortex during the forward motion of an animal wing. *J. Fluid Mech.* **587**, 471-475.
- Michalke, A. (1965). On spatially growing disturbances in an inviscid shear layer. *J. Fluid Mech.* **23**, 521-544.
- Mujres, F. T., Johansson, L. C., Barfield, R., Wolf, M., Spedding, G. R. and Hedeström, A. (2008). Leading-edge vortex improves lift in slow-flying bats. *Science* **319**, 1250-1253.
- Ng, S. (2010). Aerodynamics of a hovering hummingbird wing. PhD thesis, University of Cambridge, Cambridge, UK.
- Pennycuik, C. J. (1975). Mechanics of flight. In *Avian Biology*, Vol. 5 (ed. D. S. Farner and K. J. R.), pp. 1-75. New York, NY: Academic Press.
- Rayleigh, L. (1880). On the stability of certain fluid motions. *Proc. London Math. Soc.* **11**, 57-72.
- Rist, U. and Maucher, U. (2002). Investigations of time-growing instabilities in laminar separation bubbles. *Eur. J. Mech. B/Fluids* **21**, 495-509.
- Rodríguez, D. and Theofilis, V. (2010). Structural changes of laminar separation bubbles induced by global linear instability. *J. Fluid Mech.* **655**, 280-305.
- Schlichting, H. and Gersten, K. (2000). *Boundary Layer Theory*. Berlin: Springer-Verlag.
- Spedding, G. R. and Maxworthy, T. (1986). The generation of circulation and lift in a rigid two-dimensional fling. *J. Fluid Mech.* **165**, 247-272.
- Tobalske, B. W., Warrick, D. R., Clark, C. J., Powers, D. R., Hedrick, T. L., Hyder, G. A. and Biewener, A. A. (2007). Three-dimensional kinematics of hummingbird flight. *J. Exp. Biol.* **210**, 2368-2382.
- Usherwood, J. R. and Ellington, C. P. (2002). The aerodynamics of revolving wings II. Propeller force coefficients from mayfly to quail. *J. Exp. Biol.* **205**, 1565-1576.
- Van den Berg, C. and Ellington, C. P. (1997). The three-dimensional leading-edge vortex of a 'hovering' model hawkmoth. *Philos. Trans. R. Soc. Lond. B* **352**, 329-340.
- Videler, J. J., Stamhuis, E. J. and Povel, G. D. E. (2004). Leading-edge vortex lifts swifts. *Science* **306**, 1960-1962.
- Warrick, D. R., Tobalske, B. W. and Powers, D. R. (2005). Aerodynamics of the hovering hummingbird. *Nature* **435**, 1094-1097.
- Warrick, D. R., Tobalske, B. W. and Powers, D. R. (2009). Lift production in the hovering hummingbird. *Proc. Biol. Sci.* **276**, 3747-3752.
- Weis-Fogh, T. (1973). Quick estimates of flight fitness in hovering animals, including novel mechanisms for lift production. *J. Exp. Biol.* **59**, 169-230.